Mucus-Inspired Self-Healing Hydrogels: A Protective Barrier for Cells against Viral Infection

Raju Bej,* Corey Alfred Stevens, Chuanxiong Nie, Kai Ludwig, George D. Degen, Yannic Kerkhoff, Marina Pigaleva, Julia M. Adler, Nicole A. Bustos, Taylor M. Page, Jakob Trimpert, Stephan Block, Benedikt B. Kaufer, Katharina Ribbeck,* and Rainer Haag*

Mucus is a dynamic biological hydrogel, composed primarily of the glycoprotein mucin, exhibits unique biophysical properties and forms a barrier protecting cells against a broad-spectrum of viruses. Here, this work develops a polyglycerol sulfate-based dendronized mucin-inspired copolymer (MICP-1) with ≈10% repeating units of activated disulfide as cross-linking sites. Cryo-electron microscopy (Cryo-EM) analysis of MICP-1 reveals an elongated single-chain fiber morphology. MICP-1 shows potential inhibitory activity against many viruses such as herpes simplex virus 1 (HSV-1) and SARS-CoV-2 (including variants such as Delta and Omicron). MICP-1 produces hydrogels with viscoelastic properties similar to healthy human sputum and with tuneable microstructures using linear and branched polyethylene glycol-thiol (PEG-thiol) as cross-linkers. Single particle tracking microrheology, electron paramagnetic resonance (EPR) and cryo-scanning electron microscopy (Cryo-SEM) are used to characterize the network structures. The synthesized hydrogels exhibit self-healing properties, along with viscoelastic properties that are tuneable through reduction. A transwell assay is used to investigate the hydrogel's protective properties against viral infection against HSV-1. Live-cell microscopy confirms that these hydrogels can protect underlying cells from infection by trapping the virus, due to both network morphology and anionic multivalent effects. Overall, this novel mucin-inspired copolymer generates mucus-mimetic hydrogels on a multi-gram scale. These hydrogels can be used as models for disulfide-rich airway mucus research, and as biomaterials.

1. Introduction

Mucus, a biological dynamic hydrogel, covers all wet epithelial cells of various organs, including the airways, the eyes, the gastrointestinal tract, and the reproductive tract.[1,2] It plays a crucial role in various biological functions, such as ocular mucus protects the eyes from dryness and bacterial infections, gastric mucus mediates the coexistence of various microbes essential for digestion, airway mucus protects cells from infection caused by diverse external pathogens and cervical mucus facilitates fertilization and protects women from sexually transmitted pathogens.[3–9] Mucins (typically about 2–3% w/v) are the key component of mucus's biological hydrogels, and they determine the properties and functions of mucus.[10] Mucins exhibit a number of important characteristics, including the following: they are high-molecular-weight glycoproteins; they are highly electronegative owing to their sulfates and carboxylate groups; they feature filamentous elongated fiber-like structures; they show broad-spectrum antiviral properties; and they can undergo chain elongation and cross-linking, via disulfide linkages in their

R. Bej, C. Nie, K. Ludwig, Y. Kerkhoff, M. Pigaleva, T. M. Page, S. Block, R. Haag
Institut für Chemie und Biochemie
Freie Universität Berlin
Takustrasse 3
14195 Berlin, Germany
E-mail: rajubej@zedat.fu-berlin.de; haag@zedat.fu-berlin.de

The ORCID identification number(s) for the author(s) of this article can be found under https://doi.org/10.1002/adma.202401745

R. Bej, C. A. Stevens, G. D. Degen, N. A. Bustos, K. Ribbeck
Department of Biological Engineering
Massachusetts Institute of Technology
Cambridge, MA 02139, USA
E-mail: ribbeck@mit.edu

J. M. Adler, J. Trimpert, B. B. Kaufer
Institut für Virologie
Freie Universität Berlin
Robert-von-Ostertag-Strasse 7–13, 14163 Berlin, Germany

N. A. Bustos
Department of Mechanical Engineering
Massachusetts Institute of Technology
Cambridge, MA 02139, USA

**ADVANCED
SCIENCE NEWS**

www.advancedsciencenews.com

**ADVANCED
MATERIALS**

www.advmat.de

cysteine-rich domains, to create extended 3D network structures of very high molecular weight.[11] Mucin networks are formed through disulfide-based linkers (mesh size: 40 nm to several µm) that show unique biophysical properties.[12–15] At the macro scale, bulk viscoelastic properties control mucus's abilities to lubricate, to capture infectious pathogens via processes such as coughing and mucociliary clearance (MCC), and to protect underlying cells from viral infection using size filtration and interaction filtration owing to the presence of diverse functional groups.[16] In the case of lung diseases like asthma, chronic obstructive pulmonary disease (COPD) and cystic fibrosis (CF), the cysteine-rich domains over-cross-link, leaving diseased mucus with a higher number of disulfide bonds.[17,18] Under these compromised conditions, MCC stops and the thickened mucus becomes less effective against viruses and the infections they can cause. Mucus modulators selectively cleave certain disulfide bonds, alleviating muco-obstructive conditions.[19] In the case of cervical mucus, its properties vary depending on different stages of the menstrual cycle, controlling the selective penetration of sperm and sexually transmitted pathogens.[7]

Advancement in mucus research will therefore require understanding how native mucus regulates the biological functions described above, and how native mucus's properties change depending on health conditions. Hence, a well-characterized hydrogel capable of mimicking the biophysical properties could serve as a practical synthetic mucus model for mucus research.

Hydrogels based on native mucins have been reported in the literature as mimicking the biophysical properties of mucus, and moreover, these hydrogels have been used as model systems in various mucus research.[20–22] Mucin research today is limited by the difficulty of recovering mucin from animals and patients. There is a high degree of batch-to-batch variation within mucus samples,[23] which also suffer from low yields.

A synthetic mucus model would overcome many of the challenges associated with mucin acquisition.[24] In this regard, mucus-mimetic hydrogels based on completely synthetic materials are quite promising, especially considering their large-scale availability.[25,26] Synthetic hydrogels mimic the bulk rheology and other biophysical properties of native mucus, and they have been selectively used for various applications including mucoadhesion and testing of drug delivery matrices.[27–29] Most previously reported hydrogels only partially mimic the properties of native mucus, and the materials used for them stray far from the properties of the key component of native mucus, mucins. To be suitable for broader application, synthetic hydrogels will need to match native mucus not only in macrorheology but also on the nanoscale.[30]

Our objective is to produce mucin-inspired materials to mimic the chemical compositions, functionality and properties of native mucins, and then to use these materials as key components in the bulk-scale production of synthetic mucus in order to closely mimic the biophysical properties and biological functions of native mucus. Considering their disulfide-rich network structure, disulfide-based synthetic hydrogels can serve as a representative model system for airway mucus.

We recently developed a mucin-inspired dendronized polymer[31] (MIP) that mimics the anionic charge (sulfates and carboxylates) of native mucins, giving rise to its antiviral properties. When comparing the two, the sulfated MIP demonstrated superior antiviral activity compared to its carboxylate analogue. Hence we have further upgraded our sulfated MIP, synthesizing its analogous copolymer (**MICP**) by introducing 2-pyridyl disulfide (PDS) moieties as the crosslinking sites (**Scheme 1**) with the aim of creating disulfide-based hydrogels[32,33] using thiol cross-linkers a practical mucus-mimetic model system. We produced hydrogels on a 10-gram scale by using various polyethylene glycol-based thiol (PEG-SH) cross-linkers by varying the molecular weight (MW) and linear to branched structures.

In this article we highlight the design and synthesis of the mucin-inspired copolymer MICP and study its mucin-mimetic single-chain fiber morphology. We also investigate its biocompatibility and its antiviral properties against herpes simplex virus 1 (HSV-1) and SARS-CoV-2, as well as the mutants of the latter. Macrorheology, single particle tracking microrheology, electron paramagnetic resonance (EPR) measurements and cryo-scanning electron microscopy (cryo-SEM) were used to characterize the hydrogels in depth. Time-dependent live-cell imaging in a transwell well assay was used to investigate the impact of the hydrogels' network structure and sulfate groups on their protective properties against HSV-1 infection.

2. Results and Discussion

2.1. Mucin-Inspired Copolymer (MICP): Single-Chain Antiviral Fiber

The chemical structure of the mucin-inspired copolymer (**MICP-1**) is shown in **Figure 1a** and is comprised of two parts: the sulfated dendronized oligoglycerol methacrylate units (OGMA) that mimic the glycoprotein domain of native mucin, and the sulfated 2-pyridyl disulfide methacrylate (PDSMA) units which mimic the cysteine-rich domain. For synthesis, we first optimized the polymerization conditions to prepare relatively high-molecular-weight copolymer **P1** (pOGMA-*co*-pPDSMA) in ≈10-gram scale (Scheme S1, Supporting Information). Synthesis and characterization of **P1** are shown in the supporting information. The contribution of the individual monomers in copolymer **P1** was calculated from the ^{1}H NMR analysis (Figure S1, Supporting Information) and confirmed that the incorporation of PDSMA units was ≈10% in terms of the repeat unit. Considering ≈85% conversion of individual monomer, the molecular weight of **P1** was estimated to be 213 kDa, matching the SEC-determined molecular weight ($M_w = 203$ kDa) (Figure S2, Supporting Information) and confirming controlled radical copolymerization. Then aminolysis was performed, and the terminal dithiocarbonate groups were converted to PDS groups to get **P2** (Scheme S1, Supporting Information). The acetonide groups of **P2** were deprotected to yield **MICP-0**, which was then subjected to further sulfation to synthesize **MICP-1** (Scheme S1, Supporting Information). ^{1}H NMR (Figure S3, Supporting Information) spectrum of **MICP-0** confirmed the deprotection of acetonide groups. The shift in the methylene proton peak adjacent to sulfate groups in the ^{1}H NMR spectrum for **MICP-1** (Figure S4, Supporting Information) in comparison to **MICP-0** (Figure S3, Supporting Information) further confirmed the addition of electronegative sulfate groups. The total sulfur content in **MICP-1** was quantified by elemental analysis (Table S1, Supporting
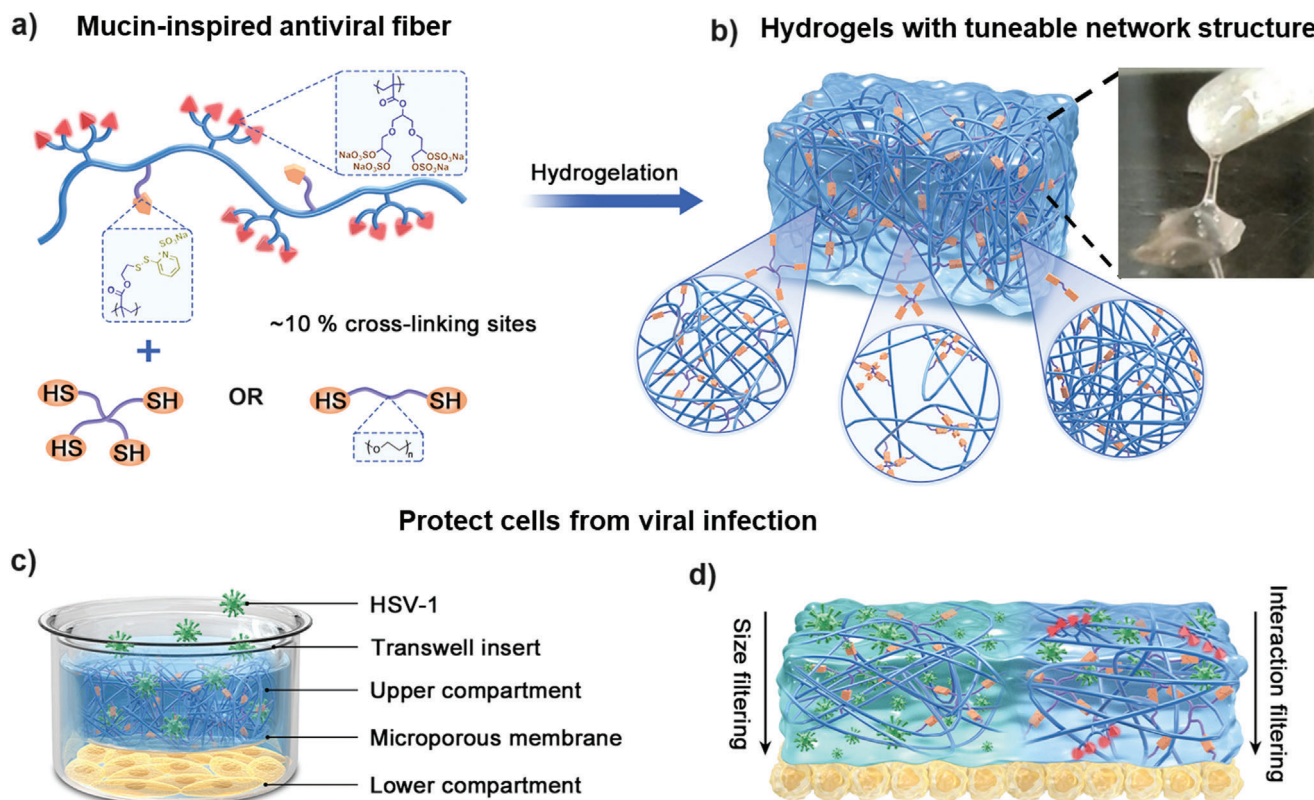
Scheme 1. a) Representative chemical structure of mucin-inspired copolymer (**MICP-1**) and its mucin-mimetic key characteristics; b) Crosslinking approach to prepare a disulfide-based hydrogel in the bulk using various cross-linker PEG-2SH_2.5, PEG-4SH_1.25 and PEG-4SH_2.5. Illustration for the tuneable microstructures of the hydrogels using different cross-linkers. Healthy sputum like synthetic hydrogel (inset); c) Transwell assay for evaluating the protective properties of hydrogels against viral infection; d) Illustration for showing size filtration and interaction filtration of the hydrogels for viral infection.

Information). The additional sulfur content indicated that sulfation happened not only on the hydroxyl groups but also in the N-center of pyridine, a conclusion that is further supported by the downfield shift of pyridine protons in the ^{1}H NMR spectrum of **MICP-1** (Figure S4, Supporting Information). Elemental analysis confirmed >90% sulfation in **MICP-1**. The estimated molecular weight of **MICP-1** from ^{1}H NMR was ≈400 kDa, matching the molecular weight obtained from size exclusion chromatography (SEC) measurement (Figure S5, Supporting Information), and falling within the molecular weight range of a mucin subunit.[34]

The overall electronegative charge of **MICP-1** was confirmed from negative zeta potential value ($\zeta = -51 \pm 6$ mV) owing to the highly sulfated functionality (Table S1, Supporting Information). The morphology of **MICP-1** in aqueous solution was investigated by cryo-electron microscopy (cryo-EM). Interestingly, **MICP-1** shows a native mucin-like elongated structure[35] (**Figure 2a** and Figure S6, Supporting Information). Cryo-electron tomography (cryo-ET) was used to determine the 3D structure and length of the fibers (Figure 2b). Manual tracing of 20 fibers resulted in a length distribution of 97.8 ± 29.4 nm. To reduce human bias, the fiber length distribution was additionally semi-automatically analyzed with Fiji[36] using 3D skeleton analysis[37] of pre-processed cryo-ET volume stacks. Of all resulting data points, noise and apparent fragmented fibers (given the poor signal-to-noise ratio)

had to be filtered out. The resulting distribution of 58 unfragmented fibers had a length distribution of 102.8 ± 29.5 nm, which is in good agreement of the manual tracing. The 10 longest fibers were 153.5 ± 36.9 nm in length which is consistent with the theoretical average length of ≈175 nm of **MICP-1** (average repeat unit = 570), calculated based on the atomic distance in the polymer chain. The observed length distribution of fibers is plausible considering the polydispersity ($Đ = 1.5$) in **MICP-1**, where PDS groups were randomly distributed throughout the polymer chain.

Cytocompatibility of the fiber **MICP-1** was tested on A549, HBE and Vero E6 cell lines, up to a polymer concentration of 5.0 mg mL^{-1}; the results suggest that **MICP-1** is biocompatible (Figure S7a, Supporting Information).

The defensive properties of native mucus arise from the broad-spectrum antiviral activities of its key component, mucins. Our group previously reported that polysulfates work against various viruses to a degree that corresponds to their amount of sulfate groups (and surface potentials).[38–40] We investigated the antiviral activity of **MICP-1** on Vero E6 cells against herpes simplex virus 1 (HSV-1) and against SARS-CoV-2 including its mutants, Delta and Omicron (BA.5). Plaque reduction assay was used to evaluate the activity of **MICP-1** against HSV-1 (Figure S8, Supporting Information). The dose-response curve showed (Figure 2c) that **MICP-1** inhibited HSV-1 with very low

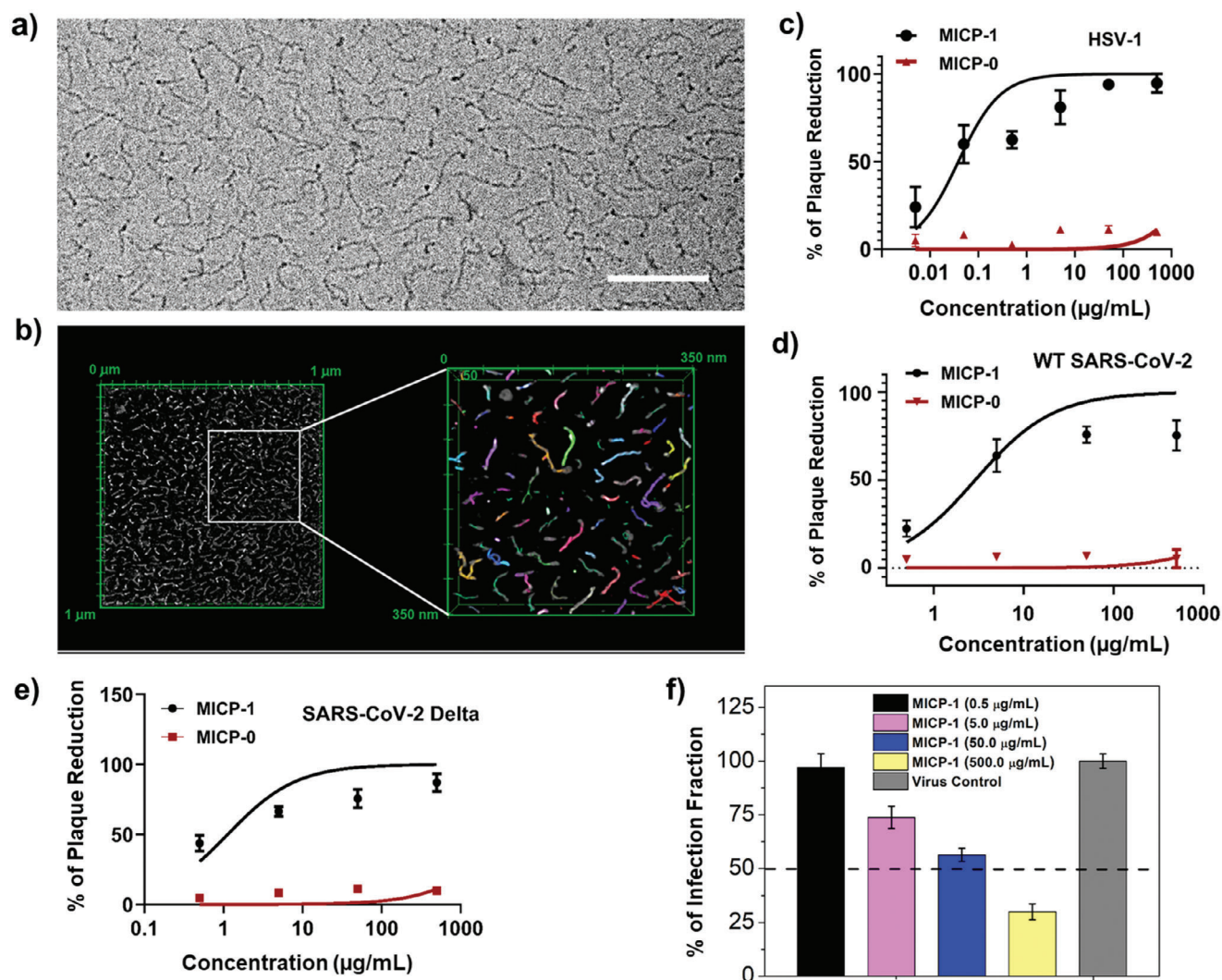**Figure 1.** a) Cryo-electron micrograph of **MICP-1** embedded in vitreous ice, showing the mucin-like, elongated fiber structure (C = 1.0 mg mL^{-1}), scale bar = 200 nm; b) Cryo-electron tomography analysis: A sub-volume of the 3D volume calculated from the tilt angle series was cut out and the fiber lengths were analyzed as described in SI; c) Dose-response inhibition of HSV-1 for **MICP-1**; d) Dose-response inhibition of SARS-CoV-2 WT variant for **MICP-1**; e) Dose-response inhibition of SARS-CoV-2 Delta variant for **MICP-1**; Non-sulfated **MICP-0** was used as control for all the cases; f) Pre-infection assay of SARS-CoV-2 BA.5 Omicron variant showing the virus inhibition activity of **MICP-1**.

half-maximal concentration (IC50 = 0.02 µg mL^{-1}, C = 50 pM). Non-sulfated copolymer (**MICP-0**) was used as control and did not show any inhibitory activities, confirming charge-dependent inhibition activity.[38]

To support its broader applicability, the antiviral activity of **MICP-1** was also evaluated against the ancestral B.1 variant of SARS-CoV-2 (SARS-CoV-2/München-1.1/2020/929)[41] and against the Delta variant on Vero E6 cells. Plaque reduction assay of **MICP-1** showed low half-maximal concentration for inhibition of SARS-CoV-2 WT (IC50 = 2.8 ± 0.5 µg mL^{-1}) (Figure 2d) and SARS-CoV-2 Delta (IC50 = 1.1 ± 0.06 µg mL^{-1}) (Figure 2e). Such low IC50 values make this compound a potential inhibitor against SARS-CoV-2; its inhibition activity is in the range reported for antibodies against SARS-CoV-2.[42,43] Non-sulfated copolymer **MICP-0** was used as control; its negligible activity against SARS-CoV-2 further confirmed the

charge-dependent SARS-CoV-2 activity of **MICP-1**. The lower IC50 value for **MICP-1** against the Delta variant, as compared to the B.1 variant, indicates its stronger activity on the former variant. This may be due to a stronger interaction by **MICP-1** with the relatively more positive receptor binding domain (RBD) of Delta versus the B.1 variant.[44] To evaluate the inhibitory effect against SARS-CoV-2 Omicron variants, we used a previously published pre-infection inhibition assay[40] and analyzed the percentage of virus infected cells based on anti-SARS-CoV-2 immunostaining. This helped to increase the accuracy of the assay as Omicron variants cause less visible plaques,[45] which reduces the reproducibility of plaque reduction assays. In this experiment, the virus (Omicron BA.5 SARS-CoV-2) was first incubated with the samples and then inoculated on Vero E6 cells for an infection of 48 h. Infected cells were stained with antibodies against SARS-CoV-2 nucleoprotein and analyzed by
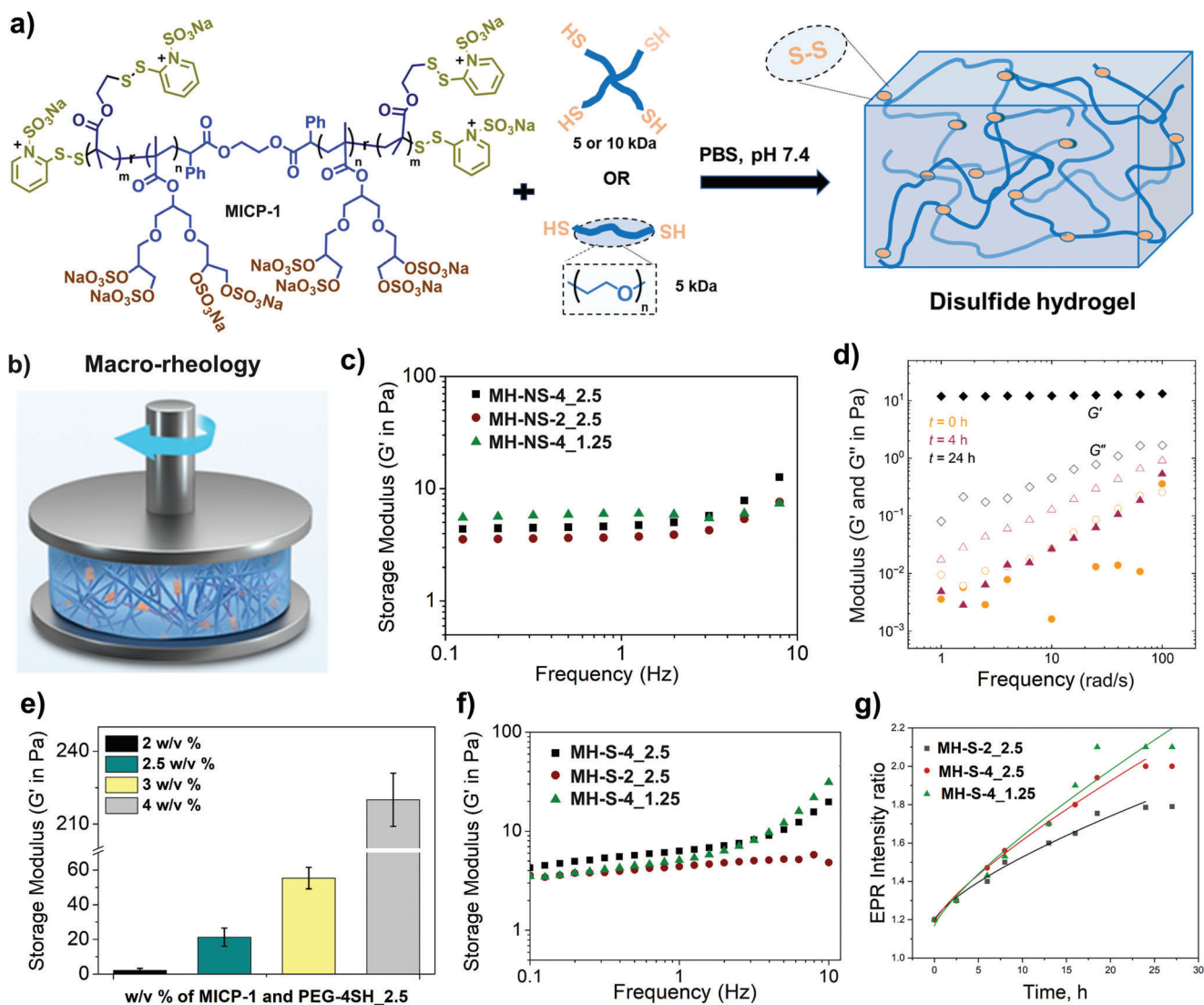
Figure 2. a) Chemical structure of mucin-inspired copolymer (**MICP-1**) and cross-linking approach via thiol-disulfide exchange chemistry to prepare mucus-mimetic disulfide hydrogels; b) Representative set up for macrorheology measurement; c) Mucus-like non-sulfated hydrogels (**MH-NS-2_2.5**, **MH-NS-4_2.5**, **MH-NS-4_1.25**) using different crosslinkers; d) Time dependent frequency sweep over the period of hydrogelation (0, 4, and 24 h using PEG-4SH_2.5 cross-linker to investigate gelation kinetics; e) Tuneable bulk-rheological properties of hydrogels by changing total w/v % of **MICP-1** and PEG-4SH_2.5 cross-linker; f) Mucus-like sulfated hydrogels (**MH-S-2_2.5**, **MH-S-4_2.5**, **MH-S-4_1.25**) using different crosslinkers; g)The time dependence of the intensity ratios of the central and high field lines of the EPR spectra of the **MICP-1** and different cross-linkers mixture. (black) PEG-2SH_2.5, (red) PEG-4SH_2.5, and (green) PEG-4SH_1.25.

fluorescence microscopy (Figure S9, Supporting Information). This setting also allows us to understand the protective effects of the compounds against virus infection if being applied prior to the infection. The reduction of infected cells in the presence of **MICP-1** (Figure 2f) confirmed its inhibition activity against the SARS-CoV-2 Omicron variant. **MICP-1** exhibits strong charge-dependent interactions with glycoproteins B and C (gB and gC) of HSV-1, as well as with the RBD of SARS-CoV-2, and thus inhibit viral infection as reported previously for the polyglycerol sulfate group.[38–40,44] In addition, long-chain polysulfate fibers of **MICP-1** probably interact via polyvalent interactions to provide enough steric shielding for excellent inhibition against multiple viruses, representing **MICP-1** as an outstanding virus inhibitors.

This synthetic mucin-mimetic fiber appears to be suitable as a novel broad-band inhibitor against multiple viruses.

2.2. Synthesis and Characterization of Mucus-Mimetic Disulfide Hydrogel

It is well understood that mucins undergo further chain elongation to form extended 3D network structures via formation of disulfide linkages in the cysteine-rich domain.[35] This leads to a dynamic hydrogel with unique rheological and biophysical properties. We were interested to test the hydrogelation properties of **MICPs** owing to its multiple 2-pyridyl disulfide groups

Table 1. Characterization of the synthetic hydrogels.

Hydrogels	Cross-linkers	Cross-linkers [w/v %]	MICPs	MICPs [w/v %]	Total solid component [w/v %]	Storage modulus [G′]	Loss Modulus [G″]
MH-NS-2_2.5	PEG-2SH_2.5	1.2	MICP-0	0.8	2.0	4.4	1.3
MH-NS-4_2.5	PEG-4SH_2.5	1.2	MICP-0	0.8	2.0	6.3	1.9
MH-NS-4_1.25	PEG-4SH_1.25	0.9	MICP-0	1.2	2.1	5.1	0.8
MH-S-2_2.5	PEG-2SH_2.5	0.93	MICP-1	1.25	2.18	3.8	2.1
MH-S-4_2.5	PEG-4SH_2.5	0.93	MICP-1	1.25	2.18	4.7	2.2
MH-S-4_1.25	PEG-4SH_1.25	0.58	MICP-1	1.6	2.18	5.9	2.9
MH-S-4_2.5_a	PEG-4SH_2.5	1.11	MICP-1	1.5	2.5	21.3	6.5
MH-S-4_2.5_b	PEG-4SH_2.5	1.3	MICP-1	1.75	3.0	55.3	7.4
MH-S-4_2.5_c	PEG-4SH_2.5	1.86	MICP-1	2.5	4.0	210	21.8

a) Storage and loss modulus at frequency 1.0 Hz.

(PDS) that can act as cross-linking sites in presence of thiol cross-linkers via the formation of disulfide bonds (Figure 1a).[33] For hydrogelation, both sulfated (**MICP-1**) and non-sulfated (**MICP-0**) copolymers were used. As cross-linkers we used linear (2-arm) and branched (4-arm) polyethylene glycol thiols (**PEG-SH**) in hopes of creating different network structures with different properties. Our cross-linkers are as follows: 4-arm polyethylene glycol thiol (**PEG-4SH_2.5**, MW = 10 kDa, average arm length per thiol = 2.5 kDa); a similar arm length linear dithiol (**PEG-2SH_2.5**, MW = 5 kDa, average arm length per thiol = 2.5 kDa); and a 4-arm PEG thiol with short arm length (**PEG-4SH_1.25**, MW = 5 kDa, average arm length per thiol = 1.25 kDa). Here we abbreviate mucus-inspired sulfated hydrogels as **MH-S** and non-sulfated hydrogels as **MH-NS**. In addition, our work defines hydrogels based on the number of arms and average arm length. Accordingly, sulfated hydrogels with PEG-2SH (MW = 5 kDa) cross-linker are abbreviated as **MH-S-2_2.5**, and hydrogels with 4-arm cross-linkers are denoted as **MH-S-4_1.25** and **MH-S-4_2.5**, respectively, for 5 and 10 kDa cross-linker. The hydrogel was formed in PBS buffer (pH ≈ 7.4) and the molar ratio of thiol groups in cross-linker and PDS groups in copolymers (**MICP**) was kept at 2:1, both to ensure the participation of all the PDS groups in cross-linking and to get more stable hydrogels.[46] In a typical procedure, copolymer and cross-linker were prepared separately in PBS buffer and mixed rapidly using a vortex for 5–10 s. Then the solution was left at room temperature for hydrogelation. Once formed, the hydrogel was rinsed with water to remove the water-soluble byproduct (2-pyridine thione), and biological experiments were performed on the purified hydrogels. The represented w/v % for hydrogelation is the total w/v % of copolymer and cross-linker.

2.2.1. Rheological Characterization: Macrorheology

The mechanical properties of a hydrogel can be described by its viscoelastic properties, which can be estimated by oscillatory rheology experiments (Figure 1b). We started by investigating the hydrogelation properties of non-sulfated copolymer (**MICP-0**) using **PEG-4SH_2.5** as a cross-linker. The hydrogelation was very fast, requiring less than 1 min. Bulk rheological properties of the hydrogel (**MH-NS-4_2.5**) were characterized (Figures S10 and S11, Supporting Information) using cone-and-plate ge-

ometry. First, a small-amplitude oscillatory shear (SAOS) strain-sweep test was conducted to determine the linear viscoelastic (LVE) region (Figure S10, Supporting Information). Then a frequency sweep (Figure S11, Supporting Information) was performed in the LVE region across the angular frequency (ω) range of 0.1−10 Hz to investigate the hydrogels' stiffness. In bulk rheological measurements, the storage modulus (G′) dominated over loss modulus (G″), confirming that the cross-linking of thiol and 2- pyridyl-disulfides (PDS) induced hydrogelation. The rheological properties of equivalent amounts of **MICP-0** and **PEG-4SH_2.5** present in hydrogel were measured separately as control (Figure S11, Supporting Information). Then the concentration of polymers (**MICP-0** and **PEG-4SH_2.5**) was tuned to prepare hydrogels of varying stiffness. It was calculated that the storage modulus (G′) of the hydrogel (**MH-NS-4_2.5**) with ≈2% w/v components was ≈6 Pa at frequency 1 Hz (Figure 1c, **Table 1**). The observed value is in the range (G′ = 1–10 Pa) of that reported previously for human healthy sputum.[47,48] We investigated hydrogelation using another branched cross-linker with a shorter arm length per thiol (**PEG-4SH_1.25**) and a linear cross-linker with the same arm length per thiol (**PEG-2SH_2.5**) and tuned the concentration to prepare the hydrogels with bulk rheology similar to airway mucus. We observed that, irrespective of the cross-linker used, an overall ≈2% w/v mixture of **MICP-0** and given cross-linker was required to achieve a mucus-like hydrogel that mimicked the solid % w/v (2–3 w/v %) of native mucus (Figure 1c, Table 1).

We then applied similar conditions to the mixture of **MICP-1** and **PEG-4SH_2.5** for hydrogelation, finding that gelation proceeded more slowly than with the non-sulfated copolymer **MICP-0**. Gelation kinetics was investigated using time-dependent bulk rheology up to 24 h (Figure 1d and Figure S12, Supporting Information). We measured biophysical parameters such as viscosity, storage modulus (G′) and loss modulus (G″) at 0, 4, and 24 h. We observed that the storage modulus gradually increased, that after a certain time it dominated over loss modulus, and that it was saturated after 14 h (Figure S12, Supporting Information). The viscosity of the solution also increased with gelation time up to the gelation point (Figure S13, Table S2, Supporting Information). We tested gelation kinetics with other cross-linkers such as **PEG-2SH_2.5** and **PEG-4SH_1.25**, finding similar trends in all cases (Figure S12, Supporting Information).

2401745 (6 of 16)

**ADVANCED
SCIENCE NEWS**

www.advancedsciencenews.com

**ADVANCED
MATERIALS**

www.advmat.de

Overall, hydrogelation was slow with the sulfated copolymers, potentially due to lower reactivity[49] of PDS groups upon the addition of electronegative sulfate groups on the N-center of pyridine groups. Moreover, the highly electronegative sulfated barriers of **MICP-1** could slow down the cross-linking reaction with the thiol groups of the cross-linkers. To test the impact of sulfated barriers in slowing down the gelation process, we synthesized a less-sulfated version of **MICP. MICP-2**, sulfated at 50%, was synthesized (Scheme S1 and Figure S14, Table S1, Supporting Information) and investigated for its gelation using **PEG-4SH_2.5** as cross-linker. It was observed that 4 h was enough time to complete the gelation. Therefore, the gelation time (Figure S15, Supporting Information) strongly depends on the degree of sulfation, and highly sulfated barriers reduced gelation speed.

MICP-1 was then used for hydrogelation in the presence of **PEG-4SH_2.5** by varying overall % w/v of the components from 2.0% w/v to 4% w/v. Frequency sweep tests of the hydrogels was performed in the LVE region and observed that the storage modulus G′ of hydrogels could be tuned by varying % w/v of polymers (**MICP-1** and **cross-linkers**) (Figure 1e). The storage modulus (G′) for 4.0% w/v polymers was ≈200 Pa and for 2% w/v was ≈5 Pa at frequency 1.0 Hz (Table 1). The hydrogel (**MH-S-4_2.5**) with ≈2% overall w/v of polymers showed a storage modulus very similar to the reported value for healthy sputum (G′ = 1–10 Pa)[47,48] (Table 1, see also Video SM01). As with non-sulfated hydrogels, we tuned the overall w/v % of **MICP-1** with other cross-linkers such as **PEG-4SH_1.25** and **PEG-2SH_2.5** to produce hydrogels similar to healthy sputum (Figure 1f and Figure S16, Supporting Information). It was observed that, irrespective of the cross-linkers used, the overall solid component required to prepare the airway-mucus-like hydrogels is ≈2% w/v (Table 1), matching the solid 2–3% w/v of mucin present in native mucus.

Further, the mesh size of hydrogels represents the void space within the hydrogel network. Such mesh networks perform key functions in healthy mucus: they help to trap pathogens, and they selectively allow external materials to pass through. The reported mesh size (ξ) for mucus is broadly distributed (40 nm to several μm) and depends on several parameters such as health condition, age, and diet. The mesh size (ξ) of a hydrogel network is directly linked to its rheological properties and can be estimated by oscillatory rheology experiments using the classical theory of rubber elasticity.[50] The theoretical calculated pore size (ξ) of the hydrogel was ≈100 nm, which is in the range of experimentally observed values for naturally occurring mucus.[9]

2.2.2. Electron Paramagnetic Resonance Measurement of Hydrogels

EPR spectroscopy is a well-known tool that can be employed to investigate processes, such as gelation, at the molecular level in various soft materials systems, including polymer hydrogels.[51] Analyzing the dynamics of the paramagnetic species within hydrogels can provide substantial information about the behavior of such systems, facilitating investigations of the kinetic profile, ranging from a sol state to the formation of a fully formed polymer hydrogel network.[52] To derive valuable information from EPR spectroscopy, one needs to introduce a stable free-radical reporter group, such as a nitroxide spin label, into the specific site of choice within the system. Therefore, we attached a spin label to the one of the terminal thiol groups of the linear cross-linker PEG-2SH (Scheme S2, Supporting Information) and further used it as a long-chain spin label connected to the main high molecular weight polymer chain, measuring the surrounding properties at some distance from the backbone. After the non-spin-labelled cross-linker (PEG-2SH_2.5, PEG-4SH_2.5 and PEG-4SH_2.5) was added to the system, we could observe the restriction in the spin label's motion, progressing with the gelation, as indicated by the broadening of the lines and redistribution of the peaks' intensities (Figure S17, Supporting Information). If the intensity ratio of the central and the high field lines decreased, the rotational correlation time – proportional to the microviscosity probed in the vicinity of this paramagnetic centers would increase. Therefore, one can observe gradual gelation over time, indicated by the time-dependent change in the EPR intensity ratio. This ratio in the EPR spectra, taken at specific time points during the gelation process, correlates well with the behavior typical of the conversion degree of the polymer solution into the gel state over time, or, in other words, for the proportion of the reacted groups (Figure 1g).[53] Indeed, the fraction of the gel phase can be expressed as follows:

$$P \approx (p - pc)^{\beta} \qquad (1)$$

where p is the fraction of reacted groups (pc at the point where the gelation is finished), β is a constant.[54] In turn, P and p can expressed as $p \approx \tau$ and $P \approx \frac{I(central\ line)}{I(high\ field\ line)}$, where τ is the time. Thus, the fraction of the formed gel is proportional to the intensity ratio of the central and the high field peaks.

As one can see from Figure 1g, the application of the cross-linkers generally results in a gradual time-dependent increase in the micro viscosity around the spin label, presumably probing it inside the pores of the hydrogel. This result is consistent with the viscosity profile over time that is observed by bulk rheology measurements. The corresponding rotational correlation times for the fully gelated states range from ≈0.9 ns for the gel cross linked with PEG-2SH_2.5, to 1.1 ns for the gel containing PEG-4SH_1.25. The rates of gelation can also be calculated from the slopes of the obtained fits, with the highest rate obtained for the longest cross-linker chains (PEG-4SH_2.5). Together with that, the time required for gelation was found to be ≈18–24 h (Table S2, Supporting Information).

2.2.3. Single Particle-Tracking Microrheology

Mucus membranes host trillion of viruses and bacteria, regulating their movement to maintain health. Understanding synthetic hydrogels' microstructure is the key to predicting how pathogens and microbes will interact with them. Single particle tracking microrheology has been widely used to gain additional insight on the biophysical properties of hydrogels on a micrometer scale.[55–59] This method includes tracking the movement of individual particles embedded in the hydrogel over time using fluorescence microscopy imaging techniques (**Figure 3a**). For this experiment, we used amine coated fluorescence polystyrene particle of size 200 nm. Since the typical size of viruses are in the range of 100–200 nm and have an overall electropositive charge,[44] the aminated particles approximately mimic how
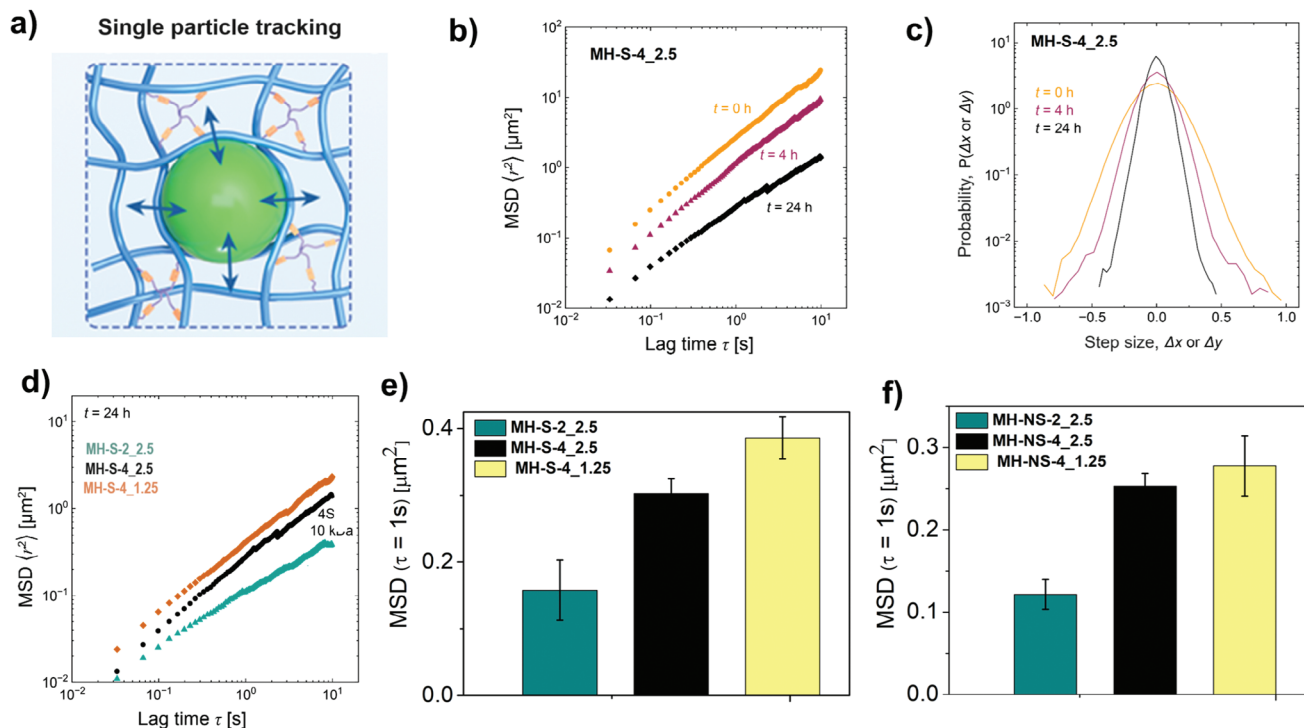
**ADVANCED
SCIENCE NEWS**

www.advancedsciencenews.com

**ADVANCED
MATERIALS**

www.advmat.de

Figure 3. Single particle-tracking micro-rheology of the hydrogels. a) Schematic representation showing movement of 200 nm amine coated fluorescent polystyrene bead through hydrogels; b) Mean-square displacement (MSD) during hydrogelation at 0, 4, and 24 h; c) Corresponding van Hove distribution at 1 s lag time; d) MSD of the 200 nm amine particles through mucus-like sulfated hydrogels with different crosslinkers at 24 h; Mean-squared displacement at 1 s of the 200 nm amine particles through mucus-like e) sulfated and f) non-sulfated hydrogels using different crosslinkers ($n = 2$).

viruses would interact with the hydrogel, to understand their movement better, prior to cell infection. The particles were added at the beginning of hydrogelation, and then the solution was injected into the custom-built flow cell microrheological setup (Figure S18, Supporting Information) and their movement was recorded over the period. Videos of length 300 frames were recorded, and particles were tracked with MATLAB using established methods,[58] yielding particle trajectories. Particle trajectories were used to calculate the mean square displacement (MSD) and van Hove distribution, related indicators of particle mobility and the network structure of the hydrogel. Ensemble-averaged mean squared displacements (MSD) for the population of particles were calculated from time-averaged individual particle trajectories as described previously,[58] and the van Hove distributions were calculated at a lag time of 33 ms.

We first investigated the gelation kinetics for the sulfated hydrogels using different cross-linkers as discussed in the bulk-rheology section. Single particle tracking measurements were performed at different time points to capture local changes during gelation up to 24 h.

First, MSD of the particles were measured (Figure 3b and Figure S19, Supporting Information) at 0, 4, and 24 h at the same time point where the bulk rheology also recorded (Figure 1). Irrespective of the cross-linker, we found that the MSD decreased with time during gelation (Table S3, Supporting Information), while the van Hove distributions show a decrease in particle step sizes (Figure 3c, Figure S19, Supporting Information).

The results indicate that movement of particles becomes restricted. Our measurements show subdiffusive behavior, indicated by an MSD approximated by a power law, $\langle \Delta r^2(\tau) \rangle = 4D_\alpha \tau^\alpha$, with exponent α less than one.[58] Because the generalized diffusion coefficients D_α of MSDs with different power law exponents cannot be compared directly, we instead report the mean squared displacement (MSD) at a lag time of 1 s, a quantity that enables direct comparison between measurements of gelation with different crosslinkers and at different curing times. Figure S20, Supporting Information shows the mean squared displacement at a lag time of 1 s taken from the MSDs shown in Figure 3c. To compare hydrogels with different crosslinkers, we measured the MSD of the hydrogels after 24 h of gelation (Figure 3d and Figure S21, Supporting Information), with mean square displacement at 1 s summarized in Figure 3e. Considering the similar macrorheology of the hydrogels, one would expect similar mesh size. However, we find different particle mobilities, suggesting that the nature of the cross-linker influences the network structures. For example, the hydrogels having similar polyethylene glycol arm length per thiol (2.5 kDa) but different architectures, in one case linear and other case branched, we found that the linear crosslinker (**MH-S-2_2.5**) resulted in lower mean squared displacement (Figure 3e), suggesting a more compact network structure. Also, branched crosslinkers with a shorter arm length per thiol (**MH-S-4_1.25**) showed larger mean squared displacements than linear crosslinkers or branched crosslinkers with longer arms, suggesting that short arm length per thiol of crosslinkers leads to more open network structures (Scheme 1b). We also investigated
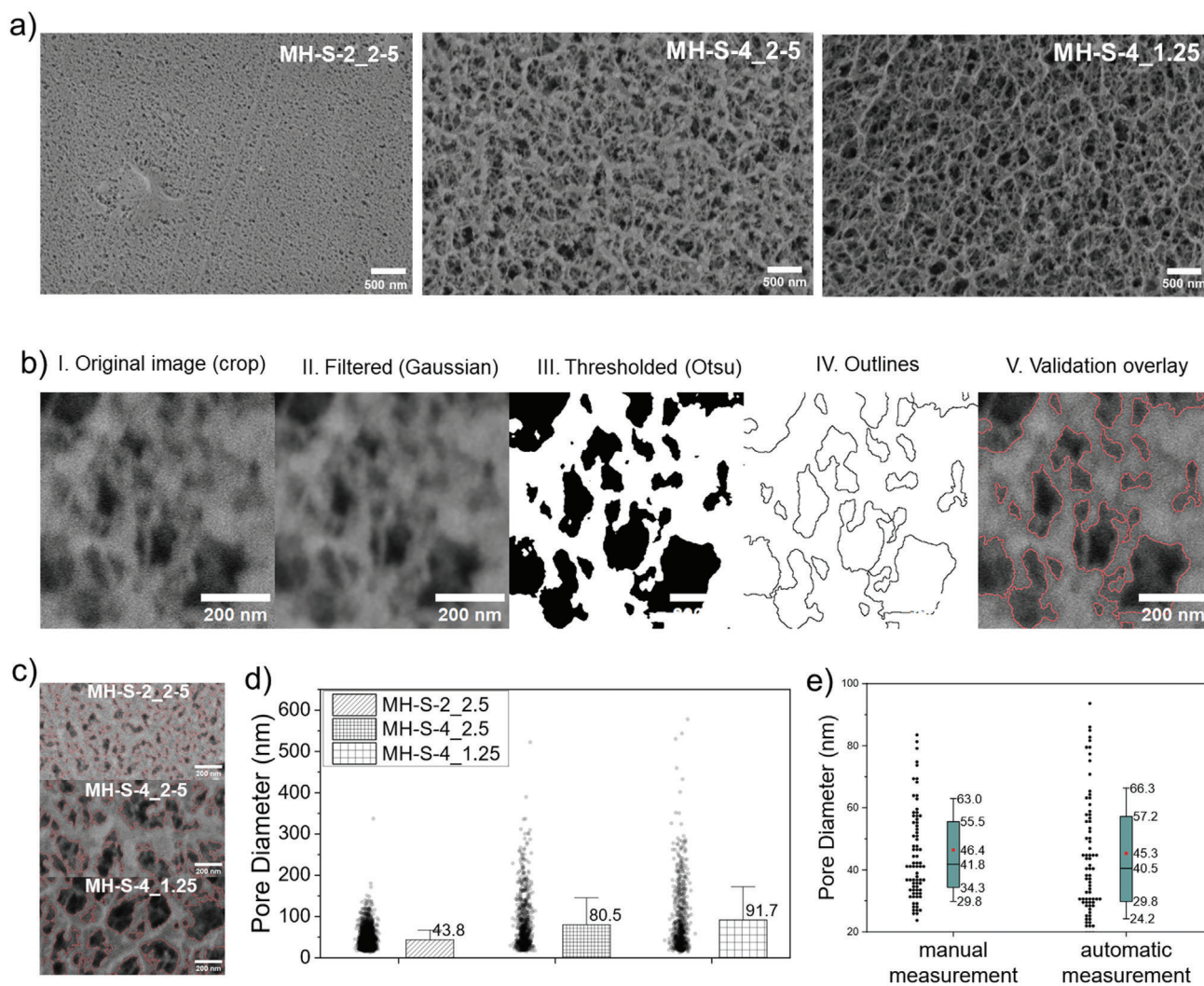
**ADVANCED
SCIENCE NEWS**

www.advancedsciencenews.com

**ADVANCED
MATERIALS**

www.advmat.de

Figure 4. a) Cryo-SEM images of sputum-like sulfated hydrogels: **MH-S-2_2.5**, **NH-S-4_2.5** and **MH-S-4_1.25** using respective crosslinkers; b) Graphical representation (I-V) of cryo-SEM image processing, analysis, and validation steps; c) Automatic image analysis for determination of pore diameter distribution for different hydrogels; d) Mean-pore size for different hydrogels; e) Comparison of 77 manually and automatic measured pore diameters for **MH-S-2_2.5**. The box plots show the mean (red dot), median (black line), 25% and 75% interval (box edges)), as well as the ± 1 standard deviation (whiskers).

particle mobility in non-sulfated hydrogels with similar rheological properties, finding a similar dependence of network structures on cross-linker structure (Figure 3f and Figure S22, Supporting Information). To further investigate the network structure of the hydrogels, we also used 1000 nm amine particles for single particle tracking measurement. The results with 1000 nm particles showed similar trends of progressively decreasing particle mobility with gelation, as shown in the SI (Figure S23, Supporting Information). Overall, our results show that gelation results in progressive restriction of nanoparticle mobility and suggest that the network structure of the hydrogels depends on the nature of the crosslinker, with linear crosslinkers and a longer arm length per thiol group resulting in denser networks and reduced particle mobility.

2.2.4. Network Structure: Cryo-Scanning Electron Microscopy

Microstructures of sputum-like hydrogels were investigated in their hydrated state, using single particle tracking measurement to characterize how the modeled particles behave. Cryo-scanning electron microscopy (cryo-SEM) images of the sulfated hydrogels with different cross-linkers were taken (**Figure 4**). Observing hydrogels with similar rheological properties, but different MSD values depending on their cross-linkers (Figure 3e,f), inspired us to investigate the network structures of the hydrogels. Here we used sputum-like sulfated synthetic hydrogels having 4 arm branched thiol (**PEG-4SH_2.5** and **PEG-4SH_1.25**) and linear di thiol (**PEG-2SH_2.5**). Cryo-SEM imaging of the hydrogels revealed porous network structures[60] for all the hydrogels

**ADVANCED
SCIENCE NEWS**

www.advancedsciencenews.com

**ADVANCED
MATERIALS**

www.advmat.de

(Figure 4a); however, network structures were dependent on the cross-linkers used.

Cryo-SEM images were analyzed with Fiji software.[36] Analysis steps (Figure 4b) are explained in the supporting information. The outlines of the detected pores were overlaid in red onto the original image for manual validation (Figure 4c). The analysis indicated that pore size for each hydrogel is heterogeneously distributed, ranging from 24 to 180 nm (Figure 4d). In general, bigger pores were observed for branched 4-arm cross-linkers than for linear cross-linkers. Among branched cross-linkers, bigger pore size was observed with shorter arm length. This could be due to linear cross-linkers' ability to orient themselves in a more flexible fashion. In contrast, branched cross-linkers cross-linked with the PDS groups more selectively, generating more void space in the network (Scheme 1b). This effect is still more prominent for even shorter arm lengths of branched cross-linker (**PEG-4SH_1.25**). Mostly likely due to its short arm length, this cross-linker results in an incomplete cross-linking of thiol groups, with less flexible fiber structures when considering steric constraints. The average pore sizes, calculated for the hydrogels **MH-S-4_2.5**, **MH-S-4_1.25**, **MH-S-2_2.5**, were ≈81, ≈92, and ≈43 nm, respectively (Figure 4d). This trend of pore size for the various hydrogels followed the similar trend that we observed in mean square displacement (MSD) experiments of 200 nm amine particles (Figure 3e). Additionally, 77 pores were measured manually, and the determined diameter was compared to the automatically determined values. The comparison showed no significant difference, proving the sufficient data quality of the automated analysis approach (Figure 4e and Figure S24, Supporting Information).

2.3. Redox-Degradable and Self-Healing Properties

Since the synthesized hydrogels are composed of disulfide bonds, they are expected to be degradable upon treatment with a reducing agent such as glutathione reduced (GSH) (**Figure 5a**).[61] In this experiment, the sulfated hydrogel **MH-S-4_2.5_a** (2.5% w/v) with 4-arm branched cross-linker was used (Table 1). For degradation studies, one part of the hydrogel was treated with 10.0 mM GSH alongside a GSH-absent control. After 24 h of treatment, the degradation of the hydrogels was investigated using macrorheology as well as single particle tracking microrheology experiments (Figure 5a). A reduction in storage modulus values was observed, indicating the degradation of some of the disulfide bonds in the presence of GSH (Figure 5b).

In parallel, the hydrogels before and after treatment with 10.0 mM GSH using single particle tracking analysis using 200 nm amine particles were tested. Results showed higher mean square displacement (MSD) of the particles at a lag time of 1s in the treated hydrogel compared to the non-treated hydrogels (Figure 5c,d and Figure S25, Supporting Information). These findings confirm that, upon treatment with GSH, some of the disulfide bonds are reduced (Figure 5a), rendering a looser network structure. This is very relevant for mucus modulator research, where testing the reduction of extra disulfide groups is important.[19] In this context, the developed hydrogels could be used as an in vitro model system for airway mucus.

Self-healing[62,63] via dynamic disulfide bonds, an important property for hydrogels, enhances their applicability in various bio-applications. For this experiment, as a representative we used **MH-S-4_2.5_b** hydrogel (3% w/v) and relatively stiffer hydrogels (Table 1). First, the strain-dependent deformation of the hydrogel was investigated by varying the percent of strain between 0.1% and 1000%. The amplitude sweep estimated the rupture point of the hydrogels at 700% strain (Figure S26, Supporting Information). Then, to examine the self-healing, extreme (1000%) and low (1%) strains were applied to **MH-S-4_2.5_b**, in alternation, up to 4 cycles (Figure 5e). Under 1000% strain, the storage modulus (G′) decreased drastically from ≈60 to ≈1 Pa (and became lower than the loss modulus (G″)), suggesting a deformed hydrogel network (with a fluid-like state). Upon reducing the strain to 1%, the ruptured network could be rapidly reorganized, as evidenced by the rapid recovery of G′ to its initial values. The dynamic nature of the disulfide bonds can be attributed to this quick recovery.

The self-healing property of the hydrogels was further investigated visually (Figure 5f). Two separate samples of **MH-S-4_2.5_b** hydrogel were prepared with green and blue color using respective color additives. Each hydrogel sample was cut with a surgical blade to give it a flush, then the two samples were brought into contact and allowed to self-heal. After 15 min, the two hydrogel samples coalesced a single hydrogel. We were then able to cut the combined hydrogel vertically, proving an efficient self-healing capacity.

2.4. Synthetic Hydrogels as Protective Barrier against HSV-1 Infection

For a successful infection, viruses must pass through the mucus barrier to reach a host cell. Therefore, evaluating the diffusion of viruses through hydrogels should provide insight to their protective capacity.

Mucus protects cells from viral infection by trapping viruses in its network structure, but also via chemical interactions (i.e., size filtration and interaction filtration) with the help of its diverse functional groups, allowing the tissue or organ to clear the virus. The inhibitory activity of **MICP-1** against many viruses inspired us further to investigate the protective barrier of its hydrogel version against viral infection. We expected that, in addition to electrostatic interactions between viruses and sulfate groups, the network structure would provide additional advantages in preventing viral infection.

A transwell assay[64–66] was used to investigate the penetration of the virus particles through the hydrogels. As a representative, here we investigated the synthetic hydrogel's protective ability in preventing HSV-1 infection of the cells (Scheme 1c). In this experiment, we investigated two factors for viral trapping: a) the impact of network structure of the non-sulfated hydrogels, using non-sulfated copolymer (**MICP-0**) as a control; and b) the impact of the hydrogels' sulfate groups, using non-sulfated hydrogel with the same cross-linker as a control. To test the impact of network structure, we prepared sputum-like non-sulfated hydrogels using three different cross-linkers, as described in section 2.2.1. The hydrogels' different pore sizes (and resulting differences in MSD values) (Figure 3f) may allow HSV-1 to infect the cells at different rates. To confirm that, the synthesized hydrogels were initially placed in a transwell, which was then placed on the Vero E6 cells on a 24-well cell culture plate. Then a solution of
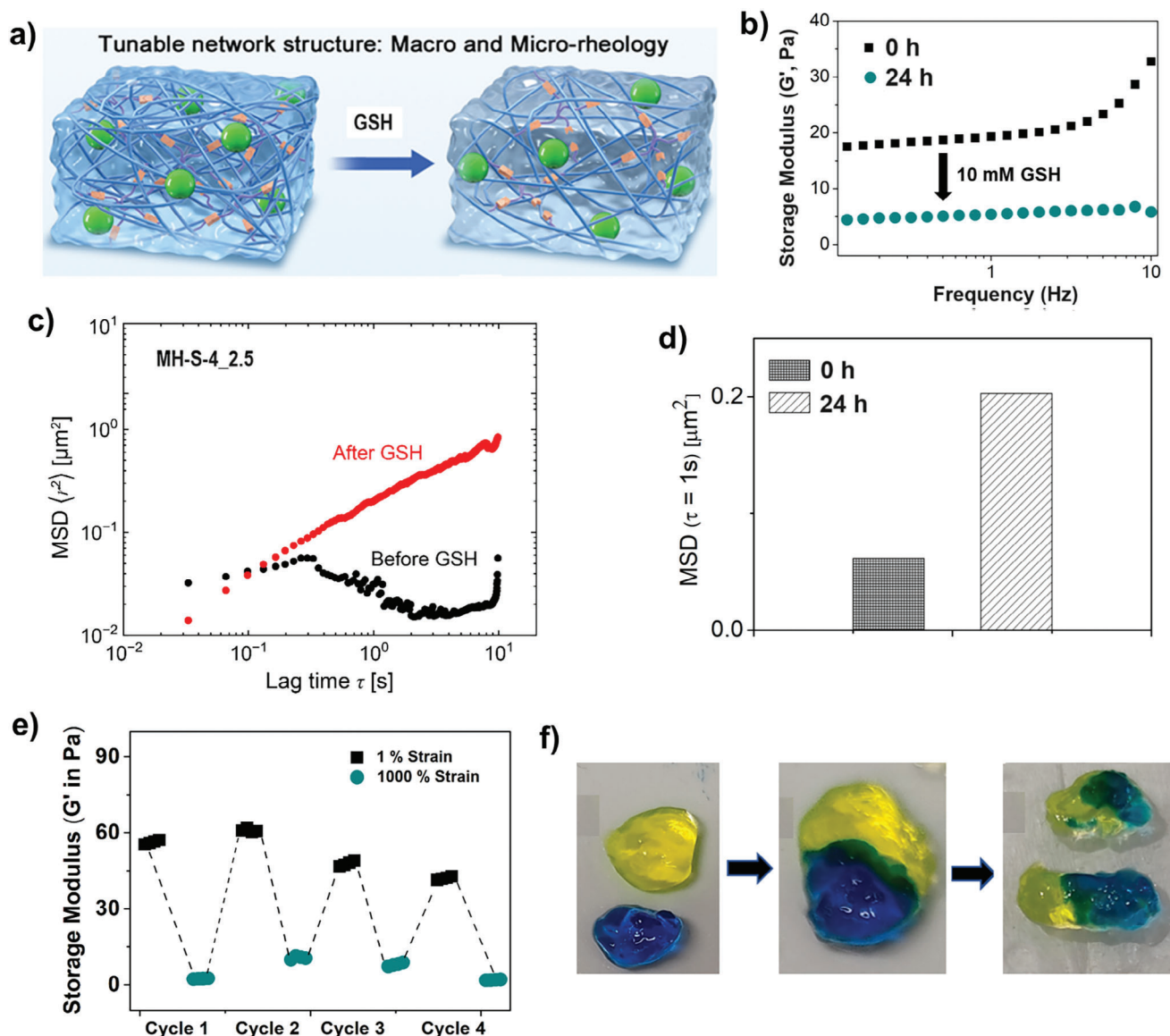
**ADVANCED
SCIENCE NEWS**

www.advancedsciencenews.com

**ADVANCED
MATERIALS**

www.advmat.de

Figure 5. a) Schematic representation showing GSH-induced degradation and network structure changes of **MH-S-4_2.5_a** hydrogel (2.5% w/v). Macrorheology and single particle tracking microrheology was used for characterization; b) Frequency sweep of the hydrogels after 24 h of GSH treatment. Black line (0 h) and cyan line (24 h); c) Mean square displacement of the 200 nm amine particles before and after 24 h of treatment with GSH; d) MSD of the particles before and after 24 h of treatment with GSH at a specific lag time of 1s. Self-healing properties of **MH-S-4_2.5_b** hydrogel (3.0% w/v).; e) frequency sweep up to 4 cycles to show the self-healing properties of the hydrogels at 1% strain and 1000% strain; f) pictorial representation of the hydrogels to show the self-healing properties visually; green and blue color from additives fluorescein sodium salt and methylene blue, respectively.

HSV-1 was added on top of the hydrogels and was allowed to pass through them to infect the underlying Vero E6 cells. We observed the infection of the cells for 72 h using time-dependent live-cell microscopy (**Figure 6**). In this experiment, the non-sulfated copolymer **MICP-0** and PBS buffer (pH ≈ 7.4) were used as control. More underlying cells were infected for the PBS buffer (Figure S27, Supporting Information) and for the non-sulfated copolymer (Figure S28, Supporting Information) than for the non-sulfated hydrogels (Figure 6a), confirming that hydrogel network structure can slow cell infection. The time intervals required for the infection of 50% of cells, for hydrogels **MH-NS-4_1.25**, **MH-NS-4_2.5**, and **MH-NS-2_2.5**, respectively, were 14,

17, and 38 h (Figure 6b). The delayed infection for **MH-NS-2_2.5** hydrogel can be attributed to its compact structures compared to other hydrogels. These results match the mean square displacement of 200 nm amine particles at lag time of 1s through the hydrogels (Figure 3f): hydrogels with smaller pore sizes show better protective ability than hydrogels with larger pore sizes (**MH-NS-4_1.25**). These results allow us to correlate network structure morphology to viral movement via pore size (Figure 6c).

To assess the biocompatibility of the synthesized hydrogels, we evaluated the cytocompatibility of **MICP-1** in Vero E6 cells up to a polymer concentration of 20 mg mL^{-1} (Figure S7b, Supporting Information). This concentration corresponds to the maximum
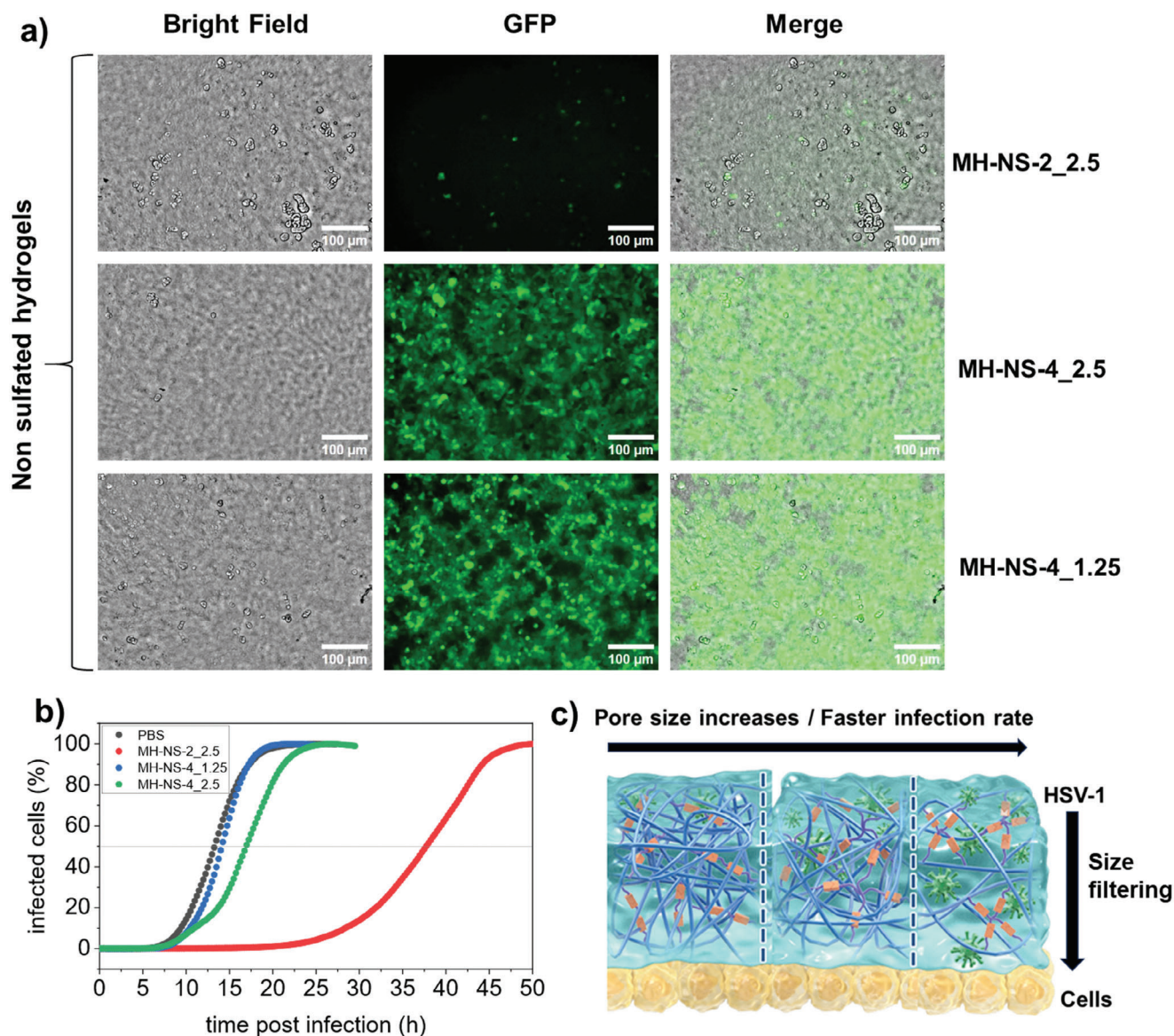
Figure 6. Transwell assay for evaluating the protective barrier ability of the non-sulfated hydrogels. Live-cell confocal microscopy to investigate HSV-1 infection in the underlying Vero-E6 cells up to 72 h/15 min. Cross-linked non-sulfated hydrogels (**MH-NS-2_2.5**, **MH-NS-4_2.5** and **MH-NS-4_1.25**) using different cross-linkers were used for investigation. a) The images of the infected cells after 20 h; For cross-linked hydrogels infection was less and, the infection get delayed confirming impact of network structure on preventing of viral infection; b) Image analysis for the time dependent quantification of the infected cells. c) Illustration of the non-sulfated hydrogels with different microstructure showing cross-linker dependent protective ability of the hydrogels. HSV-1 infection rate depends on the pore size.

amount of **MICP-1** present in the investigated hydrogels. The observation of >90% cell viability at 20 mg mL⁻¹ further confirms the biocompatibility of the hydrogels.

To understand the impact of interaction-dependent trapping, we used sulfated and non-sulfated hydrogels derived from the same cross-linker PEG-4SH_1.25, where the infection rate was fastest for non-sulfated hydrogels (Figure 6a). Since the hydrogels have similar rheological properties and show similar mean square displacement of 200 nm amine particles at lag time of 1s (Figure 3e,f), one would expect them to show similar virus-trapping abilities if the network structure played the primary role in trapping viruses. Commercially available bovine submaxillary

mucus (BSM) was used as a control. We observed the infection of the cells for 72 h using time-dependent live-cell microscopy. After 72 h, it was observed that the infection in the case of the sulfated hydrogels was negligible (**Figure 7**a), confirming complete entrapment of viruses, whereas significant infection was observed in the case of non-sulfated hydrogels (Figure 7a). This further confirms that sulfated hydrogels can protect underlying cells from infection. The time-dependent infection for sulfated hydrogels was automatically analyzed based on the GFP signal (Figure 7b).[67] The analysis for **MH-S-4_1.25** showed extremely slow infection rate (Figure 7b and Figure S29, Supporting Information). In the case of commercially available native BSM,
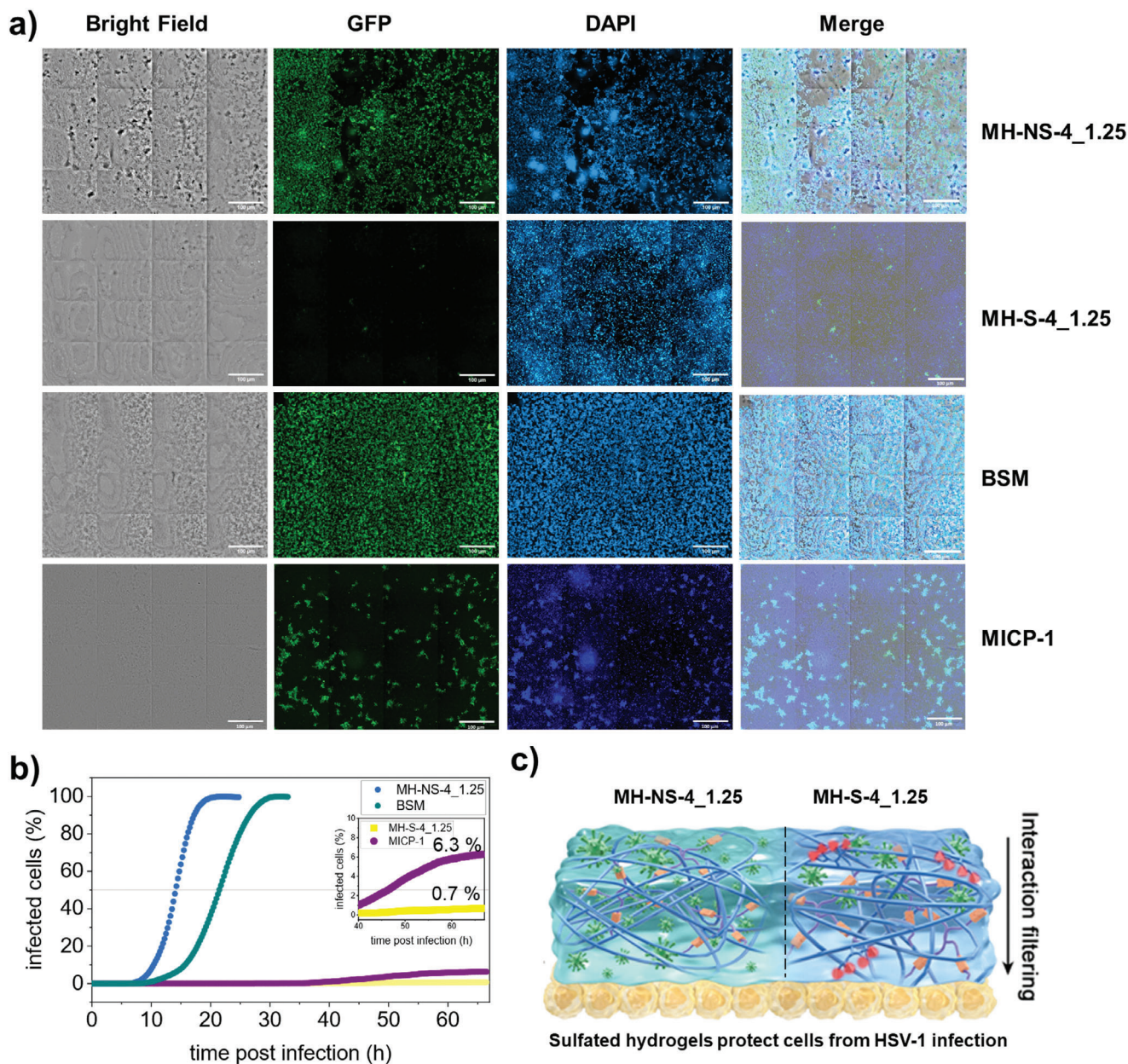
**ADVANCED
SCIENCE NEWS**

www.advancedsciencenews.com

**ADVANCED
MATERIALS**

www.advmat.de

Figure 7. Non-sulfated (**MH-NS-4_1.25**) and sulfated (**MH-S-4_1.25**) hydrogels having PEG-4SH_1.25 as cross-linker were investigated. a) Live-cell microscopy was recorded over the period of 72 h/15 min to investigate the infection in the Vero E6 cells. Negligible infection for sulfated (**MH-S-4_1.25**) hydrogels whereas cells were fully infected for non-sulfated hydrogels (**MH-NS-4_1.25**); 2 w/v % of BSM were used as control; scale bar = 100 µm. b) Image analysis for the time dependent quantification of the infected cells; c) Schematic showing negligible infection for sulfated hydrogel after 72 h of infection.

virus infection was still observed, even being delayed. We also evaluated the sulfated copolymer **MICP-1** in its non-gel state to investigate its impact on preventing viral infection. After 72 h of incubation, we observed a higher number of infected cells compared to its gel state, confirming that the hydrogel state provides better protection (Figure 7a) due to the size exclusion effects. Additionally, we quantified the time-resolved infection and found ≈6.3% infected cells for the non-gel **MICP-1**, whereas only 0.7% of cells were infected in its hydrogel state (Figure 7b and Figure S29, Supporting Information). Therefore, the sulfated hy-

drogels potently protect the cells, and this behavior arises from the combined effects of network structures and sulfated functionality (Figure 7c).[68]

3. Conclusions

Here, we developed a dendronized polyglycerol sulfate copolymer (with ≈10% of activated disulfide repeat units) that showed mucin-like elongated fiber morphology and displayed antiviral activity against various viruses. The hydrogels were prepared

on a multi-gram scale by using polyethylene glycol thiol cross-linkers. Their rheological properties can be tuned by changing weight percent per volume (% w/v) of polymers and cross-linkers, or by treating the produced hydrogel with a reducing agent. The bulk rheological properties of the hydrogels showed that ≈2 w/v % polymers produced hydrogels with similar rheological behavior to that of healthy human sputum, mimicking the overall solid content (w/v %) of mucin in native mucus. The hydrogels' microstructures were tuned by using linear or branched cross-linkers, and were investigated by single particle tracking microrheology, EPR measurements and cryo-SEM images. Hydrogels similar to healthy sputum were produced with different microstructures by varying the molecular weight and the linear to branched architecture of cross-linkers. Transwell assays were performed to evaluate the protective properties of the hydrogels against HSV-1 infection of underlying cells. The results confirmed that sulfated hydrogels completely protected the cells from HSV-1 infections, and that the protective properties resulted from the collective impact of the network structure and sulfate groups over the course of 72 h. Our mucin-inspired copolymers are not only novel biomaterials, but also have been used to prepare a mucus-mimetic hydrogel. Overall, the well-characterized synthetic hydrogels not only mimicking native mucus in bulk rheology but also mimicking selectively size- and interaction- dependent filtration. The hydrogel platform presented here can be used as a model system for disulfide-rich airway mucus and in various mucus-related disease models, including efficacy testing of mucolytic therapies with a focus on thiol and disulfide concentration.[69] We will continue working to develop this hydrogel platform into fully functional synthetic mucus model.

Supporting Information

Supporting Information is available from the Wiley Online Library or from the author.

Conflict of Interest

The authors declare no conflict of interest.

Author Contributions

C.A.S. and C.N. contributed equally to this work. R.B. synthesized the compounds. K.L. performed cryo-EM experiments. R.B., K.L., and Y.K. analyzed the cryo-EM data. C.N., J.T., and J.A. performed the SARS-CoV-2 experiments and C.N., J.T., B.K., and R.B. analyzed the data. C.N. performed the HSV-1 experiments and R.B., C.N., and Y.K. analyzed the data. R.B. and G.D. performed the macrorheology experiments and analyzed the data. M.P. performed the EPR measurement and analyzed the data. R.B., and C.S. performed the cryo-SEM measurement and S.B., and Y.K. analyzed the data. R.B., C.S., G.D., N.B., and T.P performed the single particle tracking measurements and analyzed the data. R.B. wrote the manuscript. All authors edited the manuscript. R.B., K.R., and R.H. conceptualized the project. All the authors have given approval to the final version of the manuscript.

Data Availability Statement

The data that support the findings of this study are available in the supplementary material of this article.

Keywords

[1] M. Zanin, P. Baviskar, R. Webster, R. Webby, *Cell Host Microbe* **2016**, *19*, 159.

[2] C. Werlang, G. Cárcamo-Oyarce, K. Ribbeck, *Nat. Rev. Mater.* **2019**, *4*, 134.

[3] K. M. Wheeler, G. Cárcamo-Oyarce, B. S. Turner, S. Dellos-Nolan, J. Y. Co, S. Lehoux, R. D. Cummings, D. J. Wozniak, K. Ribbeck, *Nat. Microbiol.* **2019**, *4*, 2146.

[4] B. Demouveaux, V. Gouyer, C. Robbe-Masselot, F. Gottrand, T. Narita, J.-L. Desseyn, *Sci. Rep.* **2019**, *9*, 16993.

[5] M. A. McGuckin, S. K. Lindén, P. Sutton, T. H. Florin, *Nat. Rev. Microbiol.* **2011**, *9*, 265.

[6] M. Mewe, D. Tielker, R. Schönberg, M. Schachner, K.-E. Jaeger, U. Schumacher, *J. Laryngol. Otol.* **2005**, *119*, 595.

**ADVANCED
SCIENCE NEWS**

www.advancedsciencenews.com

**ADVANCED
MATERIALS**

www.advmat.de

[7] U. Schimpf, E. Caldas-Silveira, L. Katchan, C. Vigier-Carriere, I. Lantier, G. Nachmann, S. Gidlöf, A. F. Jonasson, L. Björndahl, S. Trombotto, X. Druart, T. Crouzier, *Sci. Transl. Med.* **2022**, *14*, eabm2417.

[8] H. Boukari, B. Brichacek, P. Stratton, S. F. Mahoney, J. D. Lifson, L. Margolis, R. Nossal, *Biomacromolecules* **2009**, *10*, 2482.

[9] C. Portal, V. Gouyer, F. Gottrand, J.-L. Desseyn, *Exp. Eye Res.* **2019**, *186*, 107724.

[10] C. Ridley, D. J. Thornton, *Biochem. Soc. Trans.* **2018**, *46*, 1099.

[11] C. Ridley, M. P. Lockhart-Cairns, R. F. Collins, T. A. Jowitt, D. B. Subramani, M. Kesimer, C. Baldock, D. J. Thornton, *J. Biol. Chem.* **2019**, *294*, 17105.

[12] J. Leal, H. D. C. Smyth, D. Ghosh, *Int. J. Pharm.* **2017**, *532*, 555.

[13] R. Bansil, B. S. Turner, *Curr. Opin. Colloid Interface Sci.* **2006**, *11*, 164.

[14] O. Lieleg, K. Ribbeck, *Trends Cell Biol.* **2011**, *21*, 543.

[15] R. A. Cone, *Adv. Drug Delivery Rev.* **2009**, *61*, 75.

[16] J. V. Fahy, B. F. Dickey, *N. Engl. J. Med.* **2010**, *363*, 2233.

[17] M. A. Mall, *J. Aerosol Med. Pulm. Drug Delivery* **2008**, *21*, 13.

[18] S. Yuan, M. Hollinger, M. E. Lachowicz-Scroggins, S. C. Kerr, E. M. Dunican, B. M. Daniel, S. Ghosh, S. C. Erzurum, B. Willard, S. L. Hazen, X. Huang, S. D. Carrington, S. Oscarson, J. V. Fahy, *Sci. Transl. Med.* **2015**, *7*, 276ra27.

[19] L. E. Morgan, A. M. Jaramillo, S. K. Shenoy, D. Raclawska, N. A. Emezienna, V. L. Richardson, N. Hara, A. Q. Harder, J. C. NeeDell, C. E. Hennessy, H. M. El-Batal, C. M. Magin, D. E. Grove Villalon, G. Duncan, J. S. Hanes, J. S. Suk, D. J. Thornton, F. Holguin, W. J. Janssen, W. R. Thelin, C. M. Evans, *Nat. Commun.* **2021**, *12*, 249.

[20] C. Nowald, A. Penk, H.-Y. Chiu, T. Bein, D. Huster, O. Lieleg, *Macromol. Biosci.* **2016**, *16*, 567.

[21] C. V. Duffy, L. David, T. Crouzier, *Acta Biomater.* **2015**, *20*, 51.

[22] K. Joyner, D. Song, R. F. Hawkins, R. D. Silcott, G. A. Duncan, *Soft Matter* **2019**, *15*, 9632.

[23] A. Allen, J. P. Pearson, D. A. Hutton, A. H. Mall, R. M. Coan, L. A. Sellers, *Symp. Soc. Exp. Biol.* **1989**, *43*, 241.

[24] R. Bej, R. Haag, *J. Am. Chem. Soc.* **2022**, *144*, 20137.

[25] A. Mahalingam, J. I. Jay, K. Langheinrich, S. Shukair, S. McRaven, L. C. Rohan, B. C. Herold, T. J. Hope, P. F. Kiser, *Biomaterials* **2011**, *32*, 8343.

[26] M. T. Cook, S. L. Smith, V. V. Khutoryanskiy, *Chem. Commun.* **2015**, *51*, 14447.

[27] S. P. Authimoolam, A. L. Vasilakes, N. M. Shah, D. A. Puleo, T. D. Dziubla, *Biomacromolecules* **2014**, *15*, 3099.

[28] A. Sharma, B. Thongrom, S. Bhatia, B. von Lospichl, A. Addante, S. Y. Graeber, D. Lauster, M. A. Mall, M. Gradzielski, R. Haag, *Macromol. Rapid Commun.* **2021**, *42*, 2100303.

[29] I. Canton, N. J. Warren, A. Chahal, K. Amps, A. Wood, R. Weightman, E. Wang, H. Moore, S. P. Armes, *ACS Cent. Sci.* **2016**, *2*, 65.

[30] C. E. Wagner, M. Krupkin, K. B. Smith-Dupont, C. M. Wu, N. A. Bustos, J. Witten, K. Ribbeck, *Biomacromolecules* **2023**, *24*, 628.

[31] R. Bej, C. Nie, K. Ludwig, V. Ahmadi, J. Trimpert, J. M. Adler, T. L. Povolotsky, K. Achazi, M. Kagelmacher, R. M. Vidal, J. Dernedde, B. B. Kaufer, R. Haag, *Angew. Chem., Int. Ed.* **2023**, *62*, 202304010.

[32] R. K. Boz, D. Aydin, S. Kocak, B. Golba, R. Sanyal, A. Sanyal, *Bioconjugate Chem.* **2022**, *33*, 839.

[33] S.-Y. Choh, D. Cross, C. Wang, *Biomacromolecules* **2011**, *12*, 1126.

[34] S. P. Authimoolam, T. D. Dziubla, *Polymers* **2016**, *8*, 71.

[35] G. Javitt, L. Khmelnitsky, L. Albert, L. S. Bigman, N. Elad, D. Morgenstern, T. Ilani, Y. Levy, R. Diskin, D. Fass, *Cell* **2020**, *183*, 717 .

[36] J. Schindelin, I. Arganda-Carreras, E. Frise, V. Kaynig, M. Longair, T. Pietzsch, S. Preibisch, C. Rueden, S. Saalfeld, B. Schmid, J.-Y. Tinevez, D. J. White, V. Hartenstein, K. Eliceiri, P. Tomancak, A. Cardona, *Nat. Methods* **2012**, *9*, 676.

[37] I. Arganda-Carreras, R. Fernández-González, A. Muñoz-Barrutia, C. Ortiz-De-Solorzano, *Microsc. Res. Tech.* **2010**, *73*, 1019.

[38] P. Pouyan, C. Nie, S. Bhatia, S. Wedepohl, K. Achazi, N. Osterrieder, R. Haag, *Biomacromolecules* **2021**, *22*, 1545.

[39] C. Nie, P. Pouyan, D. Lauster, J. Trimpert, Y. Kerkhoff, G. P. Szekeres, M. Wallert, S. Block, A. K. Sahoo, J. Dernedde, K. Pagel, B. B. Kaufer, R. R. Netz, M. Ballauff, R. Haag, *Angew. Chem., Int. Ed.* **2021**, *60*, 15870;

[40] T. M. Page, C. Nie, L. Neander, T. L. Povolotsky, A. K. Sahoo, P. Nickl, J. M. Adler, O. Bawadkji, J. Radnik, K. Achazi, K. Ludwig, D. Lauster, R. R. Netz, J. Trimpert, B. Kaufer, R. Haag, I. S. Donskyi, *Small* **2023**, *19*, 2206154.

[41] R. Wölfel, V. M. Corman, W. Guggemos, M. Seilmaier, S. Zange, M. A. Müller, D. Niemeyer, T. C. Jones, P. Vollmar, C. Rothe, M. Hoelscher, T. Bleicker, S. Brünink, J. Schneider, R. Ehmann, K. Zwirglmaier, C. Drosten, C. Wendtner, *Nature* **2020**, *581*, 465.

[42] C. Wang, W. Li, D. Drabek, N. M. A. Okba, R. v. Haperen, A. D. M. E. Osterhaus, F. J. M. van Kuppeveld, B. L. Haagmans, F. Grosveld, B.-J. Bosch, *Nat. Commun.* **2020**, *11*, 2251.

[43] Z. Ku, X. Xie, P. R. Hinton, X. Liu, X. Ye, A. E. Muruato, D. C. Ng, S. Biswas, J. Zou, Y. Liu, D. Pandya, V. D. Menachery, S. Rahman, Y.-A. Cao, H. Deng, W. Xiong, K. B. Carlin, J. Liu, H. Su, E. J. Haanes, B. A. Keyt, N. Zhang, S. F. Carroll, P.-Y. Shi, Z. An, *Nature* **2021**, *595*, 719.

[44] C. Nie, A. K. Sahoo, R. R. Netz, A. Hermann, M. Ballauff, R. Haag, *ChemBioChem* **2022**, *23*, 2021006.

[45] T. P. Peacock, J. C. Brown, J. Zhou, N. Thakur, K. Sukhova, J. Newman, R. Kugathasan, A. W. C. Yan, W. Furnon, G. De Lorenzo, V. M. Cowton, D. Reuss, M. Moshe, J. L. Quantrill, O. K. Platt, M. Kaforou, A. H. Patel, M. Palmarini, D. Bailey, W. S. Barclay, *bioRxiv* **2022**, https://doi.org/10.1101/2021.12.31.474653.

[46] B. Fu, X. Wang, Z. Chen, N. Jiang, Z. Guo, Y. Zhang, S. Zhang, X. Liu, L. Liu, *J. Mater. Chem. B* **2022**, *10*, 656.

[47] M. Völler, A. Addante, H. Rulff, B. von Lospichl, S. Y. Gräber, J. Duerr, D. Lauster, R. Haag, M. Gradzielski, M. A. Mall, *Front. Physiol.* **2022**, *13*, 912049.

[48] L. Schaupp, A. Addante, M. Völler, K. Fentker, A. Kuppe, M. Bardua, J. Duerr, L. Piehler, J. Röhmel, S. Thee, M. Kirchner, M. Ziehm, D. Lauster, R. Haag, M. Gradzielski, M. Stahl, P. Mertins, S. Boutin, S. Y. Gräber, M. A. Mall, *Eur. Respir. J.* **2023**, *62*, 2202153.

[49] D. Bermejo-Velasco, A. Azemar, O. P. Oommen, J. Hilborn, O. P. Varghese, *Biomacromolecules* **2019**, *20*, 1412.

[50] B. Thongrom, M. Dimde, U. Schedler, R. Haag, *Macromol. Chem. Phys.* **2022**, *224*, 2200271.

[51] D. Hinderberger, in *EPR Spectroscopy: Applications in Chemistry and Biology* (Eds. M. Drescher, G. Jeschke), Springer, Berlin, Heidelberg, **2012**.

[52] J. P. Joly, L. Aricov, G. A. Balan, E. I. Popescu, S. Mocanu, A. R. Leonties, I. Matei, S. R. Marque, G. Ionita, *Gels* **2023**, *9*, 231.

[53] S. B. Ross-Murphy, *Polym. Bull.* **2007**, *58*, 119.

[54] M. Djabourov, *Polym. Int.* **1991**, *25*, 135.

[55] B. Dong, N. Mansour, T.-X. Huang, W. Huang, N. Fang, *Chem. Soc. Rev.* **2021**, *50*, 6483.

[56] J. A. McGlynn, N. Wu, K. M. Schultz, *J. Appl. Phys.* **2020**, *127*, 201101.

[57] B. C. Huck, O. Hartwig, A. Biehl, K. Schwarzkopf, C. Wagner, B. Loretz, X. Murgia, C.-M. Lehr, *Biomacromolecules* **2019**, *20*, 3504.

[58] C. E. Wagner, B. S. Turner, M. Rubinstein, G. H. McKinley, K. Ribbeck, *Biomacromolecules* **2017**, *18*, 3654.

[59] J. S. Crater, R. L. Carrier, *Macromol. Biosci.* **2010**, *10*, 1473.

[60] J. Kircha, A. Schneiderb, B. Abou, A. Hopf, U. F. Schaefer, M. Schneider, C. Schalld, C. Wagnerb, C.-M. Lehr, *Proc. Natl. Acad. Sci. USA* **2012**, *109*, 18355.

[61] R. Bej, P. Dey, S. Ghosh, *Soft Matter* **2020**, *16*, 11.

[62] D. L. Taylor, M. I. H. Panhuis, *Adv. Mater.* **2016**, *28*, 9060.

[63] G. A. Barcan, X. Zhang, R. M. Waymouth, *J. Am. Chem. Soc.* **2015**, *137*, 5650.

[64] J. Y. Lock, T. Carlson, R. L. Carrier, *Adv. Drug Delivery Rev.* **2018**, *124*, 34.

[65] E. Iverson, L. Kaler, E. L. Agostino, D. Song, G. A. Duncan, M. A. Scull, *Viruses* **2020**, *12*, 1425.

[66] A. Chrisnandy, D. Blondel, S. Rezakhani, N. Broguiere, M. P. Lutolf, *Nat. Mater.* **2022**, *21*, 479.

[67] Y. Kerkhoff, C. N. S. Wedepohl, V. Ahmadi, S. B. R. Haag, *MethodsX* **2022**, *9*, 101834.

[68] J. Hansing, J. R. Duke III, E. B. Fryman, J. E. DeRouchey, R. R. Netz, *Nano Lett.* **2018**, *18*, 5248.

[69] A. Addante, W. Raymond, I. Gitlin, A. Charbit, X. Orain, A. W. Scheffler, A. Kuppe, J. Duerr, M. Daniltchenko, M. Drescher, S. Y. Graeber, A.-M. Healy, S. Oscarson, J. V. Fahy, M. A. Mall, *Eur. Respir. J.* **2023**, *61*, 2202022.

2401745 (16 of 16)